A tool for empirical forecasting of major flares, coronal mass ejections, and solar particle events from a proxy of active-region free magnetic energy

David Falconer,[1,2,3] Abdulnasser F. Barghouty,[1] Igor Khazanov,[3] and Ron Moore[1]

[1]   This paper describes a new forecasting tool developed for and currently being tested by NASA's Space Radiation Analysis Group (SRAG) at Johnson Space Center, which is responsible for the monitoring and forecasting of radiation exposure levels of astronauts. The new software tool is designed for the empirical forecasting of M- and X-class flares, coronal mass ejections, and solar energetic particle events. For each type of event, the algorithm is based on the empirical relationship between the event rate and a proxy of the active region's free magnetic energy. Each empirical relationship is determined from a data set of ~40,000 active-region magnetograms from ~1300 active regions observed by SOHO/Michelson Doppler Imager (MDI) that have known histories of flare, coronal mass ejection, and solar energetic particle event production. The new tool automatically extracts each strong-field magnetic area from an MDI full-disk magnetogram, identifies each as a NOAA active region, and measures the proxy of the active region's free magnetic energy from the extracted magnetogram. For each active region, the empirical relationship is then used to convert the free-magnetic-energy proxy into an expected event rate. The expected event rate in turn can be readily converted into the probability that the active region will produce such an event in a given forward time window. Descriptions of the data sets, algorithm, and software in addition to sample applications and a validation test are presented. Further development and transition of the new tool in anticipation of SDO/HMI are briefly discussed.

1.   Introduction

[2]   NASA's Space Radiation Analysis Group (SRAG) at Johnson Space Center (JSC) is responsible for monitoring and forecasting radiation levels for astronauts. Solar particle event (SPE) forecasting is critical since SPEs can result in large, sudden, and unexpected increases in radiation levels the astronauts experience while conducting space walks (Neal Zapp Space Weather Week, 2010; available at http://helios.swpc.noaa.gov/sww/2010/wednesday/ZAPP%20SWW%202010.ppt). SRAG needs both the capability of forecasting that the necessary conditions for an SPE will not exist (all-clear forecast), and the capability of forecasting the probability that an SPE will occur. According to *Reames* [1999], SPEs come in two basic types: impulsive [3]He rich events produced by flares, and more gradual SPEs that are produced by shock fronts of fast coronal mass ejections (CMEs) [*Reames*, 1999]. For the latter, the shock front is broad, and a large part of the heliosphere can be showered in particles, resulting in only a weak longitudinal dependence of the number and strength of SPEs observed at Earth from western hemisphere source regions. The former, in contrast, eject particles into a smaller portion of the heliosphere and the source regions of impulsive SPEs observed at Earth tend to be located near where the magnetic field lines that connect the Earth to the Sun originate, ~60 degree west [*Reames*, 1999, Figure 2.3]. Some multispacecraft observations, though, indicate a wider injection spread [*Wiedenbeck et al.*, 2010; *Wibberenz and Cane*, 2006], but the distribution of source regions for impulsive SPEs observed at Earth still peaks in the western hemisphere. In any case, the first step in forecasting a SPE is to forecast its drivers: major

[1]Space Science Office, NASA Marshall Space Flight Center, Huntsville, Alabama, USA.
[2]Physics Department, University of Alabama in Huntsville, Huntsville, Alabama, USA.
[3]Center for Space Plasma and Aeronomic Research, University of Alabama in Huntsville, Huntsville, Alabama, USA.

1. REPORT DATE **07 APR 2011**	2. REPORT TYPE	3. DATES COVERED **00-00-2011 to 00-00-2011**
4. TITLE AND SUBTITLE **A tool for empirical forecasting of major flares, coronal mass ejections, and solar particle events from a proxy of active‐region free magnetic energy**		5a. CONTRACT NUMBER
		5b. GRANT NUMBER
		5c. PROGRAM ELEMENT NUMBER
6. AUTHOR(S)		5d. PROJECT NUMBER
		5e. TASK NUMBER
		5f. WORK UNIT NUMBER
7. PERFORMING ORGANIZATION NAME(S) AND ADDRESS(ES) **University of of Alabama in Huntsville,Center for Space Plasma and Aeronomic Research,Huntsville,AL,35899**		8. PERFORMING ORGANIZATION REPORT NUMBER
9. SPONSORING/MONITORING AGENCY NAME(S) AND ADDRESS(ES)		10. SPONSOR/MONITOR'S ACRONYM(S)
		11. SPONSOR/MONITOR'S REPORT NUMBER(S)
12. DISTRIBUTION/AVAILABILITY STATEMENT **Approved for public release; distribution unlimited**		
13. SUPPLEMENTARY NOTES		
14. ABSTRACT		
15. SUBJECT TERMS		

16. SECURITY CLASSIFICATION OF:			17. LIMITATION OF ABSTRACT	18. NUMBER OF PAGES	19a. NAME OF RESPONSIBLE PERSON
a. REPORT **unclassified**	b. ABSTRACT **unclassified**	c. THIS PAGE **unclassified**	**Same as Report (SAR)**	**12**	

flares (X and M class) and CMEs, especially fast CMEs. Forecasting X and M flares and CMEs would be useful for other space weather forecasters as well as for SRAG. The next step in SPE forecasting is to predict from the type, magnitude, and heliographic location of the driver, the magnitude of the resulting SPE at Earth.

[3] It would be preferable to use a physics driven model for forecasting an active region's probability of producing a major flare or CME. Because there is no agreement on how CMEs are triggered or powered, we instead use an empirical approach. From the observed performance of previous similar active regions and the measured condition of an active region's magnetic field, we determine the probability or expected rate of occurrence of X-class flares, X- and M-class flares, CMEs, fast CMEs, and SPEs to be produced by the active region. As such, the present tool is only the first step for SPE forecasting.

[4] Present major flare and CME forecasting techniques used by NOAA rely on the McIntosh active region classification scheme [*McIntosh*, 1990]. The technique works by having an observer classify an active region by sunspot presence, sunspot size, leading spot penumbra development, and sunspot distribution. There are 60 different active region classifications that can be assigned, and there are empirically determined event rates for each category. Since some of the active region classes are rare, the statistics of the empirical rates for these classes tend to be poor.

[5] It is well known that active regions that display obvious magnetic nonpotentiality (or stored free magnetic energy) are much more productive of CMEs and flares than are active regions that show little or no nonpotentiality [e.g., *Zirin and Liggett*, 1982; *Zirin*, 1988; *Canfield et al.*, 1999]. This makes forecasting based on the amount of energy stored in the coronal magnetic field a reasonable approach. This is the scientific basis of our empirical forecasting technique. We do not assume that flare and CME rates depend only on the free magnetic energy, but do assume that these rates should be correlated with the free magnetic energy. It is likely that the production rates depend on the free magnetic energy in combination with other important parameters. On one hand, a technique based solely on the free magnetic energy cannot distinguish active regions of different event productivity that have the same free magnetic energy. On the other hand, because the free magnetic energy is known to be one of the dominant determinants, we should expect a strong positive correlation between free magnetic energy and event rate without having to specifically account for the other conditions.

[6] Ideally, a direct measure of an active region's free magnetic energy in the corona should be used for forecasting purposes. Using the virial theorem, *Low* [1982] showed how this energy can be measured from an ideal vector magnetogram from a level of the active region at and above which the magnetic field is force free. However, this approach cannot yet be used because all routinely provided vector magnetograms currently available are too

inaccurate, or are of the non-force-free photosphere, or both [e.g., *Gary et al.*, 1987; *Klimchuk et al.*, 1992; *Schrijver et al.*, 2008]. Instead, we can use proxies, or indirect measures, of the free magnetic energy, which we expect to be well correlated with the free magnetic energy but with no expectation of a linear relationship between the two. One proxy of sheared or nonpotential magnetic fields are sigmoids [*Canfield et al.*, 1999], which are S or inverse S shaped coronal X-ray features. Sigmoids are not quantitative measures since a sigmoid is either evident or not, and sometimes they become evident only during the CME event; so they are of limited use for forecasting. Another proxy is the presence of a delta sunspot in the active region. A delta sunspot contains two opposite polarity umbras that share the same penumbra. This is partly the basis of the McIntosh classification scheme, but like sigmoids, an active region either does or does not have a delta sunspot. Most magnetic proxies of the free magnetic energy require a vector magnetogram (a magnetogram that maps both the line-of-sight field and the transverse field). There are several related proxy free-energy measures that are based on having strong gradients in the vertical component of the field across the neutral lines (the lines that separate the positive and negative polarities of an active region), and hence can be applied to line-of-sight magnetograms [*Falconer*, 2001; *Falconer et al.*, 2002, 2003, 2006, 2008, 2009; *Jing et al.*, 2006; *Georgoulis and Rust*, 2007; *Schrijver*, 2007]. For some unknown reason, when the Sun produces strong vertical-field gradients across a neutral line, the Sun nearly always strongly shears the magnetic field along the neutral line. The most extreme cases produce delta sunspots. Delta spots have, of course, very strong vertical-field gradients across the neutral line that separates the opposite polarity umbras. They also have very strongly sheared field along the neutral line. *Falconer et al.* [2008] have shown that the strong-gradient neutral-line measures used in the present forecasting tool is well correlated with free-energy proxies measured from the transverse field (either shear angle or net current flowing from one polarity to the other). By this correlation our strong-gradient neutral-line measure is also a proxy measure of an active region's free magnetic energy. The reason the neutral-line gradient type of measures are of special interest is the availability of large databases of consistent, good cadence magnetograms from space. SOHO/Michelson Doppler Imager's (MDI) line-of-sight magnetograph [*Scherrer et al.*, 1995], which has been taking full disk magnetograms at a cadence of 15 per day since 1996, is a prime example. To determine reliable empirical relationships between a proxy of free magnetic energy and an active region's rates of production of either flares or CMEs requires a large data set. For this study, space-based observations have several advantages over ground based observations. These include 24 h coverage, only one instrument, and no errors due to seeing. SOHO/MDI is not the only magnetograph in space; there is also the vector magnetograph on Hinode. But since Hinode was launched in 2006 as Cycle 23 was heading toward mini-

mum the number of observed active regions is much smaller. Also, the Hinode magnetograph's field of view covers only single active regions. As a result it does not consistently observe every active region on the disk, which produces biases in the data. There now is SDO/HMI, a full-disk vector magnetograph (http://hmi.stanford.edu/) that will be replacing SOHO/MDI, but it will be years before a database comparable to the current one from MDI is available. Since SOHO/MDI will be replaced, we must prepare to transition what we learn from the SOHO/MDI database to the better instrument, SDO/HMI, as discussed in section 6.

[7] Using a neutral-line gradient type of free-magnetic-energy proxy measured from line-of-sight magnetograms has the following disadvantage. The physical magnetic field of interest is the vertical magnetic field. Only when active regions are near disk center is the line-of-sight magnetic field a good approximation of the vertical magnetic field. Beyond approximately 30–40 heliocentric degrees, fictitious neutral lines can occur that are due to projection effects, and some of these can have large apparent gradients. For our empirical fitting purpose, we therefore limit our data set to only magnetograms of active regions observed within 30 heliocentric degrees. Further, our free-magnetic-energy proxy was developed for strong-field active regions where the transverse magnetic field could be measured using MSFC vector magnetograms. Thus our proxy is not designed to determine the free magnetic energy of large-scale weak-field magnetic flux concentrations in the quiet sun; these are old decaying active regions and can give rise to quiet sun prominence eruptions. However, since the most powerful flares/CMEs typically originate in strong-field active regions, concentrating on forecasting active region events is, clearly, a good starting point.

2. Description of the Databases

[8] To develop and test a forecasting tool we need to determine the empirical rates as a function of the free-magnetic-energy proxy. To this end, we need accurate flare/CME/SPE production histories of a large number of active regions and a time series of each active region's free-magnetic-energy proxy. A list of SPEs and their sources (http://umbra.nascom.nasa.gov/SEP/) has been developed by NOAA and was used for this study. As long as there are full-disk coronal images, the largest flares, X- and M-class flares, can normally each be assigned to an active region. Some C-class flares are not associated with active regions, and during solar maximum some C-class flares might not be detected because the X-ray background of the entire Sun is often mid-C level. So we limit our forecast to X- and M-class flares. CMEs are seen in SOHO/LASCO movies (http://cdaw.gsfc.nasa.gov/CME_list/). CMEs can either be frontside or backside events. We start with a flare and CME catalog from C. Balch (private communication, 2007) that used NOAA forecasters daily observations to identify source regions of flares and CMEs. This is

a labor intensive process, and made this project possible. Most CMEs, especially the more powerful ones, originate in active regions along with a major flare. From only SOHO/LASCO observations we can determine the portion of the Sun the CME likely originated from but not if the event was a frontside or backside event. In other words, when we see a CME that is seen to be rapidly growing in width, emerging above the west limb of the LASCO occulting disk, its source must be near the west limb and not near the east limb or disk center. The source region could be an active region that has just rotated over the west limb (backside), on the limb, or will soon rotate around the west limb but is on the disk of the Sun (frontside). The flare accompanying a backside CME will not be seen by GOES, while either a limb or a frontside CME will have a GOES signature. It is important to confirm the source region of a flare since during solar maximum the Sun can produce many flares, and sometimes a flare is falsely assigned to a CME. In other words a flare might occur in an active region near the east limb or disk center, and a west limb CME is seen and falsely assigned, to the wrong active region. Full-disk coronal images from various instruments SOHO/EIT, Yohkoh/SXT, GOES/SXI can be used to confirm or refute these assignments. We double checked every X- and M-class flare and CME that was important for our study, e.g., that it came from one of our active regions and had occurred during the 24 h after the time of one of our magnetograms. As such, we do not need to check flares or CMEs that are assigned to one of our active regions but occurred more than 24 h after the active region left the central disk area where we make our magnetic measurements. We have eliminated most of the falsely assigned CMEs by finding either the timing being wrong (CME seen in LASCO before flare starts) or that the CME that obviously originated near the solar limb but was assigned to a central-disk active region flare. Occasionally a quiet Sun prominence eruption (CME) was falsely associated with a nearby active region.

[9] The time series of each active region's free-magnetic-energy proxy was determined using an automated algorithm that extracts from full-disk MDI magnetograms strong magnetic field areas, identifies them with NOAA's active regions, and then measures our proxy of free magnetic energy. This automated capability is critical to our new forecasting tool. We have applied this algorithm to all full-disk MDI magnetograms; however, for purposes of the results and analysis presented in this work, the effective end date is December 2004 which corresponds to the end date of Balch's flare/CME database. Our focus is to evaluate flare and CME rates as functions of only our proxy of free magnetic energy of isolated active regions. There are cases, however, when two or more NOAA active regions are included in a single, extracted strong-field magnetic area. For simplicity, these particular cases have been excluded as they represent only ~15% of the magnetic islands corresponding to active regions. We also exclude strong-field magnetic areas that are not NOAA active regions, since Balch's flare/CME database only

includes events from NOAA active regions. The combined database we have developed runs from the date of the first MDI active-region magnetogram (10 May 1996) through the last entry of the flare/CME catalog (24 December 2004). The data set consists of ~40,000 magnetograms from ~1300 active regions with known flare, CME, and SPE production histories. Using this large combined database, we are able to discern power law dependence between our proxy of the free magnetic energy of an active region and the active region's flare rate, its CME rate, its fast CME rate, and its SPE rate. These rates were incorporated into our beta forecasting tool, currently being tested by NASA/SRAG. We also plan to apply these techniques to SDO/HMI full-disk magnetograms.

2.1. Magnetic Measurements Database

2.1.1. NOAA Active Regions, Magnetic Islands, and Magnetic Measures

[10] In a previous study [*Falconer et al.*, 2009], we manually selected a subfield of view of a full disk MDI magnetogram that encompassed only the active region of interest. This selected subfield was shifted from magnetogram to magnetogram to track solar rotation and thus develop a time series of magnetic measures for each active region. This is a reasonable approach for a sample of 44 active regions, but applying this technique to a large sample would be very time consuming. Also, a forecasting tool would need to be able to automatically identify a reasonable subfield of view to enclose one active region. We have developed an automated algorithm to use for both scientific studies and forecasting. This allows us to apply various conditions depending on the quality of the inputs. The inputs are MDI magnetograms and NOAA active region lists (http://www.swpc.noaa.gov/ftpdir/forecasts/SRS/). The technique identifies contiguous sets of pixels with strong magnetic field, which appear on plots like islands in a sea; so we call them "magnetic islands." We rather call them magnetic islands than active regions, since they can contain zero, one or more active regions. Our free-energy proxy is tailored to active regions, which are the predominant source of flares and CMEs, so we need to remove from the list those magnetic islands that are not active regions as described below. A subfield of view of the full-disk magnetogram is needed to evaluate our magnetic measures. This is accomplished using a polygon such that all magnetogram pixels enclosed by the polygon are used to evaluate our magnetic measures. The addition of a portion of the quiet sun has negligible effect on our magnetic measures, but the inclusion of a portion of another active region could lead to an overestimation of an active region's free magnetic energy. Therefore, any portion of another magnetic island is excluded leaving each magnetic island enclosed in a polygon that encloses one, and only one island. Some magnetic islands include two or more NOAA active regions; they are excluded from the present study because of complications they pose. We have plans for future studies to refine the tool to include them. At present the

forecast tool treats them as one active region for evaluation and forecasting event rates using the conversion function obtained from isolated active regions.

2.1.2. Magnetic Island Identification Algorithm

[11] To identify active regions the following algorithm is used. We mask the limb (>0.95 R_S) to avoid limb effects. We then smooth the logarithm of the magnitude of the line-of-sight magnetic field with a Gaussian smoother [*Gonzalez and Woods*, 1992] that has a full width at half max of 12 pixels. We apply a 25 G threshold to the 5 min average MDI magnetograms and 35 G to the noisier 1 min average MDI magnetograms. This process leaves a large number of strong field islands including active regions, plage, and ephemeral active regions. Narrower Gaussian smoothers were tried initially, but often active regions would be divided into two separate parts. We increased the width so that we would not divide active regions into two different islands. As a consequence the number of islands having multiple NOAA active regions was increased.

[12] To eliminated magnetic islands that are not sunspot active regions because they are too small or the field is too week, we keep only islands that fulfill two conditions: (1) the island has a maximum line-of-sight field greater than 750 G and (2) the island has an area of over 50 MDI pixels (~200 arcsec^2). The numerical values of all these thresholds and parameters were empirically determined, and can be modified by the forecaster, but are used consistently to develop the database. All islands that meet these requirements were numbered.

2.1.3. Enclosing Magnetic Islands With Polygons

[13] Next, we enclose each island with a polygon in which all pixels are measured in evaluating the magnetic measures. The initial polygons are rectangles that barely enclose the islands, and are recorded as a list of five vertices (the bottom right corner is both the first and last vertex of the list). For cases where two polygons overlap, the overlapping area is subdivided so that each polygon encloses one and only one magnetic island. The key requirement of this process is that neither polygon encloses any portion of the other magnetic island as this would affect our magnetic measures. This is done by changing the vertices list. The code first determines if either magnetic island extends into the overlapping area. If no magnetic island extends into the area, the first magnetic island examined has its polygon modified. If one magnetic island extends into the area then the other polygon vertices are modified so as to exclude the overlapping area. If both islands extend into the polygon then both vertices' lists are modified by adding the vertices that described the "coastline" of the second island. This process is repeated for all overlapping areas.

2.1.4. Assigning NOAA Active Region Numbers to Magnetic Islands

[14] The NOAA active-region list for the day is then used to assign active region numbers. This is done in two steps. First, if the location that NOAA gives for the active region falls inside one of the magnetic island's polygons,

it is assigned that number, or numbers for the case of multiple active regions. Second, if the NOAA-reported location of an active region falls outside, but near a magnetic island without an assigned NOAA active region number, it is assigned the number. The second is most common for small active regions, since NOAA's locations are given in whole heliographic degrees.

2.1.5. Evaluating Magnetic Measures and Proxies

[15] For each magnetic island, each magnetic measure is evaluated. The proxy of free magnetic energy takes advantage of the observation that nonpotential or sheared magnetic field tends to build up along magnetic neutral lines, and magnetic neutral lines that vector magnetograms observe to have strong gradients across them in the vertical magnetic field nearly always have strongly sheared horizontal field along them. By integrating the gradients of the vertical magnetic field along the neutral lines we obtain the weighted length of the strong-gradient neutral line (denoted by $^{L}WL_{SG}$). To evaluate it with a line-of-sight magnetogram (Figure 1), we use the line-of-sight approximation treating the line-of-sight field as if it were the vertical field and limit the analysis to active regions within 30 heliocentric degrees of disk center. Unable to measure the horizontal field with a line-of-sight magnetogram, we instead use the transverse potential magnetic field extrapolated from the line-of-sight magnetic field to limit our neutral lines to neutral lines with strong horizontal magnetic fields. This is done as described by *Falconer et al.* [2006, 2008] where the magnetic measure $^{L}WL_{SG}$ is defined as

$$^{L}WL_{SG} = \int |\nabla_{\perp}B_{los}|dl, \qquad (1)$$

where $\nabla_{\perp}B_{los}$ is the transverse gradient of the line-of-sight magnetic field, and the integral is taken over all neutral-line increments dl (Figure 1) on which the potential transverse field computed from the magnetogram is >150 G. The above is applied only to that part of the MDI magnetogram that is enclosed by the polygon that encloses the magnetic island. This integral is evaluated numerically by dividing the neutral line into multiple increments, each roughly a pixel in length. For each increment we determine the potential transverse field and transverse gradient at the midpoint of the increment by interpolation from the values for each pixel of the magnetogram. For those increments with potential field larger than 150 G the product of the increment's length and gradient is summed over all strong-field neutral lines.

[16] Other magnetic measures are also determined at this stage. Two other important magnetic measures used in this paper are (1) the magnetic area, A_m, defined as

$$A_m = \int_{|B_{los}| > 100\,G} da, \qquad (2)$$

where $|B_{los}|$ is the strength of the line-of-sight magnetic field and the integral is taken over all areas of the mag-

netogram for which $|B_{los}| > 100$ G, and (2) the length of the strong-field neutral line, $^{L}L_S$, defined as

$$^{L}L_S = \int_{pB_t > 150\,G} dl, \qquad (3)$$

where the integral is taken over all neutral-line increments dl on which the potential transverse field, pB_t, computed from the magnetogram is >150 G. An example of an MDI active-region magnetogram and its strong-field intervals of neutral lines is shown in Figure 1.

[17] For each magnetic island, the vertices of the polygon used, the associated NOAA active region number, and the magnetic measures are included in our database for analysis. The NOAA active region number is used only to associate flares, CMEs, and SPEs for obtaining our forecasting curves (section 2.2); this step is not needed for the forecasting. Currently, this database extends from May 1996 through the present, but due to the event catalog ending in December 2004 (section 2.2), in this paper we use only data for May 1996 through December 2004.

2.2. Flare/CME/SPE Database

[18] NOAA has both a Flare/CME list (C. Balch, private communication, 2007) and an SPE list (http://umbra.nascom.nasa.gov/SEP/). The flare/CME database runs through December 2004, and the SPE database had its last entry in 2006 (the last recorded SPE of Cycle 23). The flare list has assigned individual flares to particular NOAA active regions, and for each flare it lists whether it occurred together with a CME. The magnitude and start time of the flare as well as the speed of the accompanying CME is recorded in our database. The SPE list has active region assignment, start time of flare, magnitude of associated flare, and magnitude of SPE for >10 MeV protons with flux above 10 pfu (1 pfu = 1 particle/cm^2/s/sr). We cross reference these two databases with our MDI magnetic island list, using active region numbers, to compile, for each active region, an event history as well as a magnetic measures history to produce the combined data set, which is the basis of our forecasting curves.

[19] We confirmed the association of each flare, CME and SPE in the database that could affect our results (i.e., that occurred in an active region within 24 h of a central disk magnetogram). This was done by checking LASCO, SXT, EIT, and SXI movies, and GOES timing found at (http://sxi.ngdc.noaa.gov/ and http://cdaw.gsfc.nasa.gov/CME_list/). The most common correction to the database came from finding that a CME that originated from just beyond the limb (backside event) had been falsely associated with a flare occurring in an active region near disk center.

3. Forecasting Technique

[20] To determine the expected empirical event rate as a function of our free-magnetic-energy proxy we use the isolated active regions in the combined database (MDI
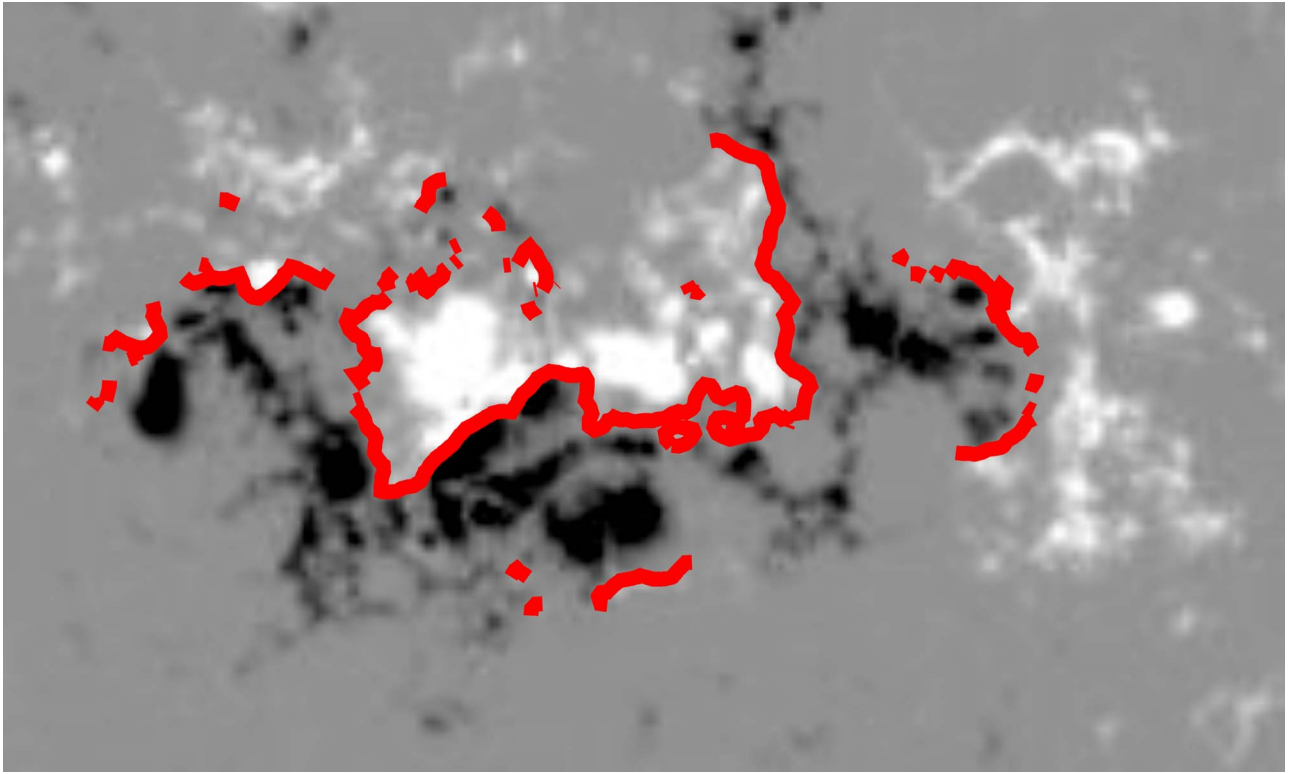
Figure 1. An active-region line-of-sight magnetogram (AR 9077 14 July 2000) from MDI and the strong-field neutral lines from which our proxy of the active region's free magnetic energy is evaluated. An active region is composed of strong positive (white) and negative (black) magnetic field concentrations. Separating the positive and negative field are magnetic neutral lines, at which magnetic field of opposite polarity can cancel. The strong-field intervals of the neutral lines are colored red (see text).

magnetic measures combined with NOAA event history as described in section 2). We use only magnetic islands with only one assigned NOAA active region, and only when the active region is within 30 heliocentric degrees of disk center. These two conditions are applied since we need to avoid cases where our measurements sum over more than one active region, and we want to include only cases where projection effects are acceptably small [*Falconer et al.*, 2008]. Our magnetic measure, $^{L}WL_{SG}$, is designed to indirectly measure the free magnetic energy of strong-field active regions, that is active regions in which enough of the neutral line has potential transverse field that is strong (>150 G). This measure is not a good proxy of the free magnetic energy of old decaying active regions that have lost their sunspots. To exclude these decaying active regions we require that the length of the strong-field neutral line, L_S, divided by the square root of the magnetic area of the active region is greater than 0.75. Our set of magnetic islands (now measured active regions) that fulfill these conditions consists of 39,977 magnetograms from 1329 active regions observed between 10 May 1996 and 25 December 2004, which period spans part of the solar cycle 22–23 minimum phase and the maximum phase of solar cycle 23.

[21] To determine the dependence of an event rate on our proxy of free magnetic energy, where event rate can mean X flare rate, X and M flare rate, CME rate, fast-CME rate (fast CMEs are CMEs with plane-of-sky velocity of greater than 800 km/s), or SPE rate, we bin our sample in bins of increasing $^{L}WL_{SG}$. For each bin we determine the average $^{L}WL_{SG}$, the number of CMEs, X and M flares, fast CMEs, and SPEs that occur during the 24 h period after the time of the active-region magnetogram. The number of counted events divided by the number of active-region magnetograms in a bin is the 24 h event rate for that bin. Using Poisson statistics [*Sachs*, 1978], we then determine, for each bin and event type, the 1-sigma uncertainty in the event rate.

[22] We divided our data into 40 equally populated bins (~1000 active-region magnetograms per bin) for reasonable statistics per bin. For each kind of event the average $^{L}WL_{SG}$, event rate, and uncertainty of the event rate are log-log plotted in Figure 2. At this point, to convert a new active region's measured $^{L}WL_{SG}$, to the active region's
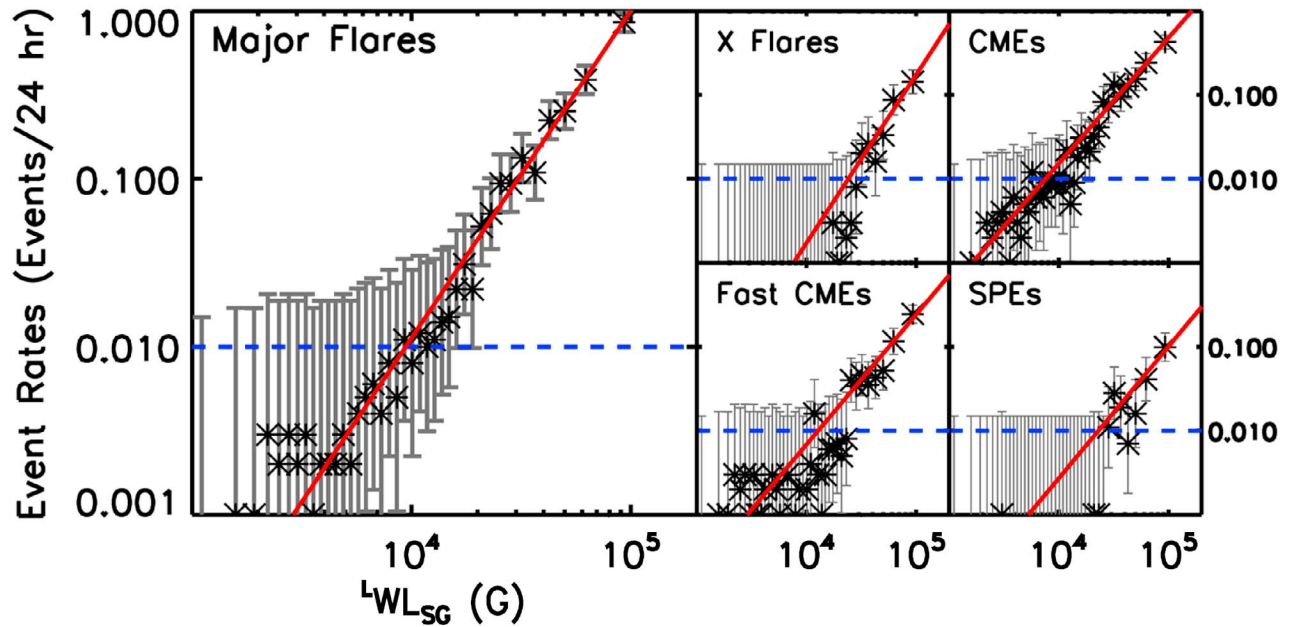
Figure 2. Log-log plots of event rates versus the free-magnetic-energy proxy. Each bin value (asterisks), its rate uncertainty (I), and the power law fits (red lines) are shown. Blue dashed lines are 0.01 events per 24 h threshold used in the fits (see text).

forecasted event rate, we could use a lookup table, assigning the active region the expected event rate for the bin that $^{L}WL_{SG}$ value falls in. For an active region of this range of $^{L}WL_{SG}$ the expected event rates are determined from our database. We rejected this technique since the event rates fluctuate from bin to bin, not consistently monotonically increasing. This would result in ranges of $^{L}WL_{SG}$ where as $^{L}WL_{SG}$ increases the predicted rate would decrease. Instead, and since we do have an approximate power law relationship (Figure 2), we decided to fit the data with a power law and estimate the forecasted rate based on the measured $^{L}WL_{SG}$, its uncertainty, the power law fit and the uncertainty in the power law fit. The power law fit, for each type of event, is determined only from those bins with event rates of 0.01 events per 24 h (>10 events per 1000 magnetograms). Only bins with rates greater than 0.01 are used because for bins with no events the upper limit of the 1-sigma uncertainty is just over 0.015/d. The fit is in the form

$$R = a\left(^{L}WL_{SG}\right)^{b}. \qquad (4)$$

[23] The fit parameters, their uncertainties, and the fit's reduced chi-square value are given in Table 1. The best fit is for major flares, with the fits for the other event types having larger reduced chi-square values and typically larger uncertainties. The uncertainty in *a* is minimized by dividing $^{L}WL_{SG}$ by 50,000 G so that the log-y inter-

cept is near the centroid of the fitted bins. Relative to the uncertainties in measured values of $^{L}WL_{SG}$, the uncertainties in the fitting parameters dominate the uncertainty in the forecast event rate and are symmetrical in log-space, resulting in a multiplicative factor of the rate (e.g., for a 1-sigma uncertainty of a factor of 2, the 1-sigma range extends from twice the rate given to half the rate given).

[24] We can choose the value of $^{L}WL_{SG}$ below which we make an all-clear forecast. This all-clear ceiling value of $^{L}WL_{SG}$ also determines the fraction of the sample in the all-clear range of $^{L}WL_{SG}$. Figure 3 shows an example all-clear ceiling of 0.05 events per 24 h for each type of event. Table 2 lists the percent of the sample below the ceiling, together with the rate of the bin of greatest $^{L}WL_{SG}$. For this example, we use a threshold rate of 0.05 events per day for the chance of an event to be considered non-negligible. The semilog scale of Figure 3 is used to emphasize that only for a small number of active regions (large $^{L}WL_{SG}$) is the probability of an event nonnegligible.

4. Validating the Active-Region Forecast

[25] As a preliminary test of the validity of our forecasting method, we have divided our sample into two groups separated chronologically; all the observations on a given day or before belong to the first group and all the observations after that day belong to the second group. From the first group we have determined the fitting parameters "*a*" and "*b*" of equation (4). With these fitting

Table 1. Parameters for the Power Law Fits

Event Type	$\log_{10} a$	b	Reduced Chi-Square Value
X and M flares	−9.75 ± 0.03	1.95 ± 0.14	0.21
X flares	−10.77 ± 0.11	2.00 ± 0.58	0.39
CMEs	−7.81 ± 0.04	1.50 ± 0.16	0.31
Fast CMEs	−8.36 ± 0.07	1.55 ± 0.29	0.43
SPEs	−8.84 ± 0.12	1.57 ± 0.59	0.44

Table 2. All Clear Fraction and Maximum Rates for Different Event Types

Event Type	Percent All Clear	Max Rate
X and M flares	77%	0.87
X flares	95%	0.15
CMEs	78%	0.43
Fast CMEs	89%	0.21
SPEs	97%	0.09

parameters we forecast the expected event rates of major flares for the second group. Major flares were selected as the event type for this preliminary test based on them being the most numerous type of event, and hence having the best statistics.

[26] The second group is then binned in 10 equally populated bins based on these forecast rates, and for each bin the average forecasted rate is compared to the average actual rate. Figure 4 shows a plot of such a comparison for before and after 30 June 2002, which date roughly puts 70% of the active-region magnetograms in the first group and 30% in the second. Similar results were obtained using other dividing dates. This shows that our forecasting method works quite well. The error bars are calculated with Poisson statistics to estimate the likely range of the actual event rate. Similar to the fitting procedure of the forecast curves in Figures 2 and 3, in Figure 4 only the five bins with forecasted rates greater than 0.01/d are plotted.

For the highest forecasted rate bin, the error bars are logarithmically small due to the large number of M and X flares. In any particular bin there are active regions whose rates are larger or smaller due to other factors. We expect to improve the forecast by identifying and using secondary forecast measures, as we allude to in the discussion.

5. Full-Disk Forecasting Tool

[27] For forecasting an expected event rate or probability of event for the whole face of the Sun, we need to forecast the expected rate of each active region on the solar disk. The selection limitations we placed on our combined data set to determine empirical event rates, namely, within 30 heliocentric degrees, and only one active region per a strong-field magnetic island (see section 3) are dropped. These restrictions were needed to derive the most accurate parameters for power law fits (Table 1), but the active
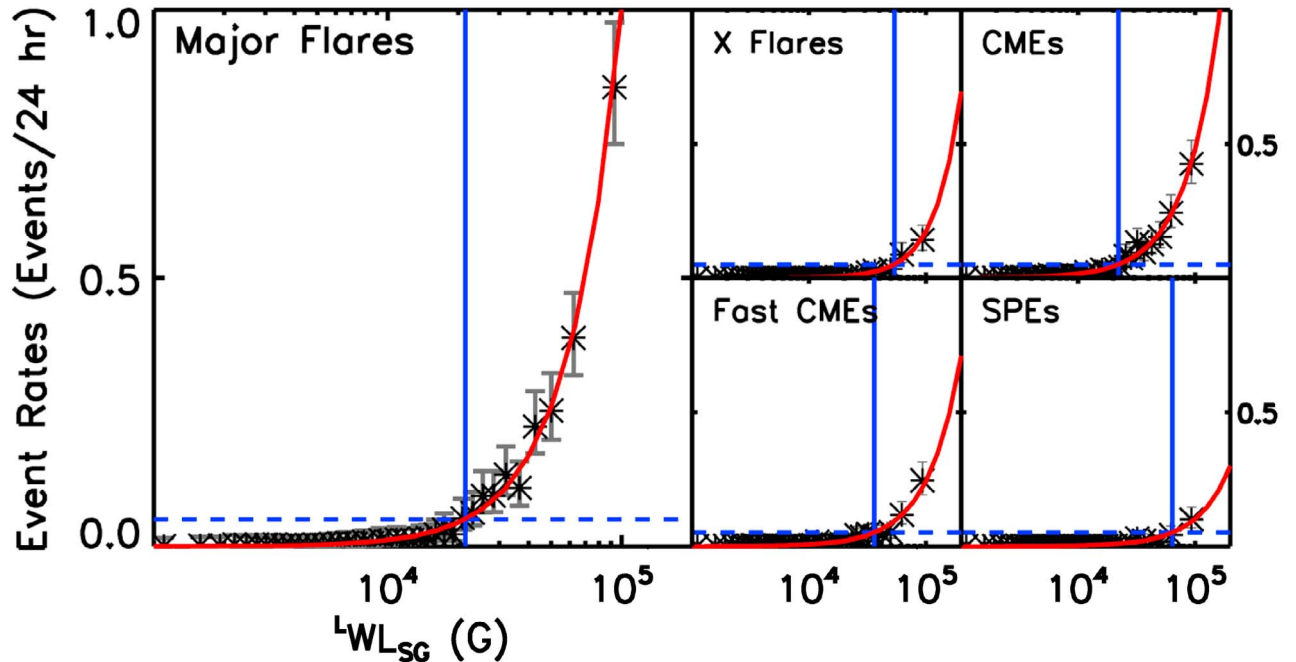

Figure 3. Same as Figure 2 but in linear-log space. Blue horizontal lines depict the 5% threshold (see text), and the blue vertical lines are the corresponding threshold values of $^L\mathrm{WL_{SG}}$.
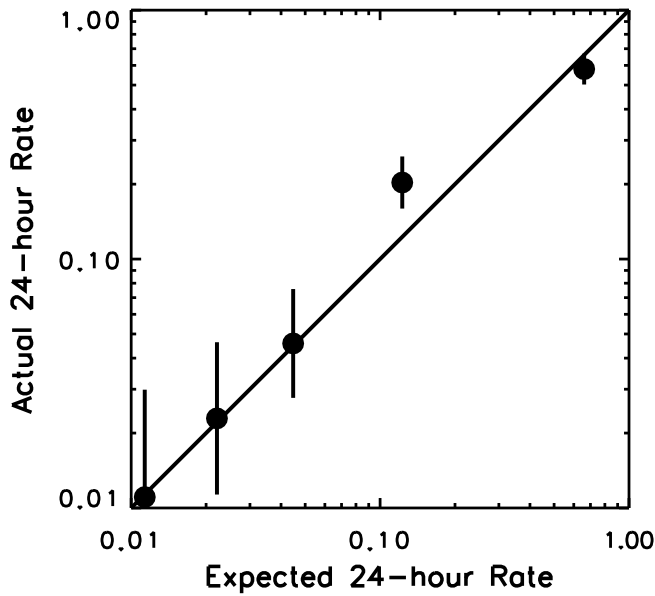
Figure 4. Log-log plot of the actual rates versus the expected rates for major flares (see text for details). The actual rates equal the expected rate on the diagonal line.

regions beyond 30 degrees cannot be ignored for full-disk forecasting. Ignoring them would result in an underestimation of the actual full-disk event rate. The forecasts for these are more uncertain since fictitious neutral lines (neutral lines in the line-of-sight field but not in the real vertical magnetic field) will cause occasional erroneously large $^{L}WL_{SG}$, and thus erroneously large forecasted rates. Users are thus warned when the active region is beyond 30 heliocentric degrees and the measured values of $^{L}WL_{SG}$ are suspect. They are also cautioned in the event that a strong magnetic field area with multiple active regions is being treated as one active region. This last change, however, is likely to have small effects since typically either most active regions in the group have little free energy, and so the group has a small $^{L}WL_{SG}$ and thus a negligible overall expected event rate, or one active region in the group dominates $^{L}WL_{SG}$ as well as the event rate. Only when there are two or more active regions with comparable and moderate to large $^{L}WL_{SG}$ will we overestimate the probability of an event. Further, the case of two nonpotential active regions that are close and likely connected by magnetic loops, the actual event rate might differ from the case of two active regions that are well isolated from each other. We plan to determine in future research whether their event rates change but for now assume there is no effect.

[28] Sample results of the present forecast tool are shown in Figure 5 for 29 October 2003. Shown on the top left of Figure 5 is the name of the MDI magnetogram and all NOAA active regions listed for the day. On the top right, the date and time of the magnetogram are listed.

The table on the bottom lists the results for each magnetic island with NOAA active region and full disk estimated event rates and probability of events along with their uncertainties. Each strong-field magnetic island is identified and enclosed in a polygon. In the center, a full-disk MDI magnetogram with line-of-sight field (scaled between ±250 G) is shown where the center of the disk (red plus sign) and the 30° radius central disk (red circle) where the magnetic measures are most accurate are plotted. NOAA active regions (the reported heliographic location of each active region is marked with a red asterisk) are assigned to appropriate strong-field magnetic islands as described in section 3. In this particular case, a NOAA active region on the west limb is unassigned, and four active regions are assigned to magnetic island 1. (Note that the enclosing polygon in this case is an example of where the polygon is not a rectangle due to the small magnetic island number 3.) The magnetic measures are determined for all strong-field magnetic islands with at least one assigned NOAA active region number. We color code each magnetic island using the color scheme (green, yellow, and red), with thresholds at 0.01 and 0.1 major flares a day, to indicate the level of risk forecast. Strong field magnetic islands without NOAA active regions assigned are colored pink if within 30 heliocentric degrees of disk center and blue if outside. For cases of two or more active regions assigned to the same polygon, a plus sign is added to the active region number with the largest size. For active regions beyond 30 degrees, an exclamation point is added to indicate that the active region is outside the 30° radius central disk, and the predicted rates should be used with extra caution.

[29] Besides giving forecasts for each individual strong magnetic island we also give a forecast for the entire disk. This is done by summing up the individual magnetic islands rates. For this reason for each kind of event, the assigned multiplicative uncertainty for the Disk forecast is the multiplicative uncertainty of the highest forecasted rate. Normally, only the event rate of one magnetic island, dominates the full-disk rate. All event rates are given only to one significant digit.

[30] These rates can then be converted into all-clear event probabilities as functions of the length of time t of the forecast interval using the following relation:

$$\text{Prob}(t) = 100\% \left(e^{-Rt} \right), \tag{5}$$

where Prob (t) is the absolute probability of having no events in time t, and R is the event rate [*Wheatland*, 2001; *Moon et al.*, 2001]. Note than while R can be greater than 1 per day, Prob (t) will only asymptotically approach 0% as R gets large. Reporting the expected event rate has an advantage over reporting only the event probability; unlike the probability measure, for a given rate R the number of events increases linearly with the length of the time interval. The disk all-clear probabilities are listed with uncertainties in the last two rows, and are shown graphically on the "threat gauge," to the right of the MDI

Figure 5. Sample output of the new forecast tool for 29 October 2003 (an extremely active day of Cycle 23).

magnetogram, with red showing the chance of an event, green the chance of no event, and yellow showing the range of uncertainty in the all-clear probability. The uncertainty in the all-clear probabilities tends to be large relative to the all-clear probability or the event probability (100% minus the all-clear probability), whichever is smaller, and is also larger for X-class flares and SPEs compared to M and X flares or CMEs due to poorer statistics (Figure 5). The forecasted event probabilities span several decades but most are actually negligibly small. The particular day shown in the Figure 5 is during the passage of the Halloween 2003 active regions, one of the most event active times during the last cycle and is not a typical day.

6. Discussion

[31] We have presented a description of a new forecasting tool developed for and currently being tested by NASA's Space Radiation Analysis Group at JSC, which is

responsible for monitoring and forecasting of radiation exposure levels of astronauts. The new empirical forecasting tool is based on a proxy of an active region's free magnetic energy that can be measured from a line-of-sight magnetogram and that has strong predictive ability for the rates of active region's production of M and X flares, CMEs, fast CMEs (>800 km/s), and Solar Particle Events. The tool uses the empirically determined power law relationship between our proxy of active-region free magnetic energy and the event rate. The tool is automated: it can take any full-disk MDI magnetogram, isolate strong-field areas, identify the strong-field areas with NOAA active regions, extract magnetic measures, make forecasts for individual magnetic islands as well as for the full Sun, save an entry for a database, and output a forecast plot (Figure 5). This forecast tool is the first quantitative tool based on a magnetic measure delivered to a space weather forecasting organization (NASA/SRAG) for potential operational use. In contrast the *McIntosh* [1990] active-region forecast scheme, used by NOAA, is based on

60 prescribed active-region categories; the category assigned to an active region is determined by human inspection of photosphere images of the active region.

[32] The present algorithm assumes that no other parameter than our free-energy proxy affects an active region's event rate. It is likely that active-region event rates do depend on other parameters. We plan to incorporate secondary measures (e.g., previous flare activity), that, when properly combined with $^L WL_{SG}$, will give a more accurate forecast than using $^L WL_{SG}$ alone. We believe our large data set will allow such investigations in the future, and thus allow future improvements to our tool.

[33] For SPE forecasting, the algorithm can be improved by the addition of more physics. The empirical SPE rate is found, presently, for active regions observed within 30 heliocentric degrees from the disk center. Work by *Reames* [1999], and others have shown dependence of SPE occurrence at Earth on the longitude of the source of the driving eruption, which our algorithm does not include. Most SPEs at Earth come from active regions in western longitudes. With MDI line-of-sight magnetograms the error in the measurement of $^L WL_{SG}$ from active regions beyond 30 degrees from disk center could easily swamp the longitudinal dependence, but with HMI vector magnetograms the longitudinal dependence of the rate of production of SPEs observed at Earth by active regions can be taken into account. Also, coupling the forecast flare/CME rate for an active region with heliospheric models should, in principal, result in an improved forecast of the chance of an SPE at Earth.

[34] The new forecasting technique, however, has two weaknesses: lack of magnetic observations of active regions on or behind the limb and the fact that no attempt at forecasting quiet-region prominence eruption has been made. The lack of limb observations can be partially addressed for west limb events which are more likely to produce SPEs than east limb events [*Balch*, 2008] (26 West Limb, 2 East limb, out of a sample of 165 SPEs) by using the last (furthest west) good evaluation for longer forecasts. Forecasting for active regions on the East limb would need to use forecaster estimates based on STEREO observation (http://stereo-ssc.nascom.nasa.gov/), farside helioseismology, and recent history of the active region rotating onto the disk. Placing magnetographs in the Earth/Sun L4 and L5 points would supply the observations needed for using this forecasting technique for active regions near and beyond the east limb. The development of a forecasting technique for quiet-region prominence eruptions would improve forecasting of CMEs. The associated flares though are normally weak, and these CMEs rarely produce SPEs, so forecasts of X and M flares or SPEs will not be improved significantly.

[35] The tool is presently based on using MDI line-of-sight magnetograms, but now that SDO with HMI is launched, we will be able to make the tool better due to HMI's advantages over MDI. These advantages include vector magnetograms, higher resolution, reduced latency, and faster cadence. The vector magnetograms can be deprojected to disk center (convert line-of-sight and transverse field to vertical and horizontal magnetic fields) and so remove the line-of-sight approximation, and thus more accurately measure our proxy of free magnetic energy in active regions further from disk center. Also, several proxies of free magnetic energy that are measured from the horizontal magnetic field component will be obtainable from the HMI vector magnetograms. To determine if any of these proxies are better than $^L WL_{SG}$ and to develop a usefully large database will take many years of observations. The higher resolution will tend to result in HMI measuring a larger gradient along the neutral line than does MDI for the same active region, at the same time. By using either the overlap between MDI and HMI observations, or if both do not observe enough active regions, by chaining through either SOLIS or Hinode vector magnetograms this effect can be calibrated out so that the MDI database can be used for HMI magnetograms. SOHO/MDI is currently operating with reduced data throughput and does not bring down and make calibrated data readily available. During the solar minimum this is not so critical since active region driven events are rare and soon it will be replaced by HMI, which will have short latency. Some delay (several hours) is acceptable since $^L WL_{SG}$ tends to evolve on timescales of a day or more.

References

Balch, C. C. (2008), Updated verification of the Space Weather Prediction Center's solar energetic particle prediction model, *Space Weather*, *6*, S01001, doi:10.1029/2007SW000337.

Canfield, R. C., H. S. Hudson, and D. E. McKenzie (1999), Sigmoidal morphology and eruptive solar activity, *Geophys. Res. Lett.*, *26*, 627, doi:10.1029/1999GL900105.

Falconer, D. A. (2001), A prospective method for predicting coronal mass ejections from vector magnetograms, *J. Geophys. Res.*, *106*, 25,185, doi:10.1029/2000JA004005.

Falconer, D. A., R. L. Moore, and G. A. Gary (2002), Correlation of coronal mass ejection productivity of solar active regions with measures of their global nonpotentiality from vector magnetograms: Baseline results, *Astrophys. J.*, *569*, 1016, doi:10.1086/339161.

Falconer, D. A., R. L. Moore, and G. A. Gary (2003), A measure from line-of-sight magnetograms for prediction of coronal mass ejections, *J. Geophys. Res.*, *108*(A10), 1380, doi:10.1029/2003JA010030.

Falconer, D. A., R. L. Moore, and G. A. Gary (2006), Magnetic causes of solar coronal mass ejections: Dominance of the free magnetic energy over the magnetic twist alone, *Astrophys. J.*, *644*, 1258, doi:10.1086/503699.

Falconer, D. A., R. L. Moore, and G. A. Gary (2008), Magnetogram measures of total nonpotentiality for prediction of solar coronal mass ejections from active regions of any degree of magnetic complexity, *Astrophys. J.*, *689*, 1433, doi:10.1086/591045.

Falconer, D. A., R. L. Moore, G. A. Gary, and M. Adams (2009), The "main sequence" of explosive solar active regions: Discovery and interpretation, *Astrophys. J.*, *700*, L166, doi:10.1088/0004-637X/700/2/L166.

Gary, G. A., R. L. Moore, M. J. Hagyard, and B. M. Haisch (1987), Nonpotential features observed in the magnetic field of an active region, *Astrophys. J.*, *314*, 782, doi:10.1086/165104.

Georgoulis, M. K., and D. M. Rust (2007), Quantitative forecasting of major flares, *Astrophys. J.*, *661*, L109, doi:10.1086/518718.

Gonzalez, R., and R. Woods (1992), *Digital Image Processing*, Addison-Wesley, Reading, Mass.

Jing, J., H. Song, V. Abramenko, C. Tan, and H. Wang (2006), The statistical relationship between the photospheric magnetic properties and the flare productivity of active regions, *Astrophys. J.*, *644*, 1273, doi:10.1086/503895.

Klimchuk, J. A., R. C. Canfield, and J. E. Rhoads (1992), The practical application of the magnetic virial theorem, *Astrophys. J.*, *385*, 327, doi:10.1086/170942.

Low, B. C. (1982), Magnetic field configurations associated with polarity intrusion in a solar active region: I. The force-free fields, *Sol. Phys.*, *77*, 43, doi:10.1007/BF00156094.

McIntosh, P. (1990), The classification of sunspot groups, *Sol. Phys.*, *125*, 251, doi:10.1007/BF00158405.

Moon, Y.-J., G. S. Choe, H. S. Yun, and Y. D. Park (2001), Flaring time interval distribution and spatial correlation of major X-ray solar flares, *J. Geophys. Res.*, *106*, 29,951, doi:10.1029/2000JA000224.

Reames, D. V. (1999), Particle acceleration at the Sun and in the heliosphere, *Space Sci. Rev.*, *90*, 413, doi:10.1023/A:1005105831781.

Sachs, L. (1978), *Applied Statistics: A Handbook of Techniques*, Springer, New York.

Scherrer, P. H., et al. (1995), The solar oscillations investigation—Michelson Doppler imager, *Sol. Phys.*, *162*, 129, doi:10.1007/BF00733429.

Schrijver, C. J. (2007), A characteristic magnetic pattern associated with all major flares and its use in flare forecasting, *Astrophys. J.*, *655*, L117, doi:10.1086/511857.

Schrijver, C. J., et al. (2008), Nonlinear force-free modeling of a solar active region around the time of a major flare and coronal mass ejection, *Astrophys. J.*, *675*, 1637, doi:10.1086/527413.

Wheatland, M. S. (2001), Rates of flaring in individual active regions, *Sol. Phys.*, *203*, 87, doi:10.1023/A:1012749706764.

Wibberenz, G., and H. V. Cane (2006), Multi-spacecraft observations of solar flare particles in the inner heliosphere, *Astrophys. J.*, *650*, 1199, doi:10.1086/506598.

Wiedenbeck, M. E., et al. (2010), Observations of a ^{3}He-rich SEP event over a broad range of heliographic longitudes: Results from STEREO and ACE, *AIP Conf. Proc.*, *1216*, 621, doi:10.1063/1.3395943.

Zirin, H. (1988), *Astrophysics of the Sun*, Cambridge Univ. Press, Cambridge, U. K.

Zirin, H., and M. A. Liggett (1982), Delta spots and great flares, *Sol. Phys.*, *113*, 267, doi:10.1007/BF00147707.

A. F. Barghouty and R. Moore, Space Science Office, NASA Marshall Space Flight Center, Mail Code VP62, Huntsville, AL 35812, USA.

D. Falconer and I. Khazanov, Center for Space Plasma and Aeronomic Research, University of Alabama in Huntsville, Huntsville, AL 35899, USA. (david.a.falconer@nasa.gov)